International Scholarly Research Network
ISRN Civil Engineering
Volume 2012, Article ID 345979, 11 pages
doi:10.5402/2012/345979

Research Article

A Barotropic Model of the Red Sea Circulation

Mohamed M. El-Shabrawy, Khaled M. Fasseih, and Mamdouh A. Zaki

Faculty of Engineering, Cairo University, Giza 12613, Egypt

Correspondence should be addressed to Mohamed M. El-Shabrawy, mmshabrawy@gmail.com

Received 11 January 2012; Accepted 2 February 2012

Academic Editors: I. Raftoyiannis and N. Xie

A linear depth-averaged numerical model of the horizontal barotropic circulation of the Red Sea is developed. The flow considered is incompressible, quasi-steady and free from vertical buoyancy currents and horizontal density currents. The model predicts general water circulation as affected by friction stresses at the irregular Red Sea bottom and coastal features, variable Coriolis force, vertical, and lateral turbulent friction, and seasonal non-uniformity of wind stress at the sea surface. The implicit finite-difference solution of the boundary value problem is verified with previous solutions for a rectangular constant-depth sea and for an elliptical lake with uniformly-sloping bottom topography. The model output is shown as plots of seasonally-averaged mass-transport vectors and circulation streamlines in the Red Sea basin.

1. Introduction

The Red Sea is 2040 km length, 280 km averaged width, and 491 m averaged depth. Also, its latitude extent between 12°N and 28°N warrants an effective and variable Coriolis force, the β-effect [1]. The two-dimensional models for this effect on ocean currents were devised for constant-depth rectangular basins [2, 5]. The combined action of depth variation and the β-effect on the two-dimensional currents were also modeled [1, 3, 4]. The driving wind was assumed constant [3, 4] although it is variable [1]. The bottom friction was modeled by linear mass-transport dependence [3, 4] while lateral turbulent friction was neglected. The lateral turbulent friction was modeled, in [1], by linear dependence on mass- transport dependence. This assumption had no effect the order of the elliptic partial differential equation governing the depth-integrated circulation streamline. Analytical solutions were obtained, in [1], for constant depth basins with variable Coriolis parameter and spatially-variable wind stress distribution. All of these two-dimensional models [1, 3–5], have neglected lateral turbulent friction.

This two-dimensional model considers the manner by which barotropic circulation in the Red Sea is affected by its irregular bottom bathymetry, latitude variation of the Coriolis force, vertical and lateral turbulent friction stresses, and seasonal variation of the surface wind stress. The mass and momentum conservation equations are vertically integrated and combined to form a single partial differential equation for the mass transport stream function. Bottom friction is modeled by linear mass- transport dependence while lateral turbulent friction has a third order mass- transport dependence. The external driving force acts at the sea surface as a non-uniform seasonally-averaged wind stress. The governing equations of the three-dimensional flow are modified by the model assumptions of incompressible and hydrostatic flow. This allows the derivation of the governing equations of the two-dimensional baro-tropic (homogeneous sea water density) and quasi-steady circulation. The depth-integrated equations are hence manipulated to result in a bi-harmonic equation of the mass-transport stream function.

A finite difference scheme formulation of the bi-harmonic equation over a Cartesian mesh with variable grid size is derived. The model is verified versus simple cases of known analytical solutions. The test cases include both constant and variable depth basins with uniform and variable wind stress distributions. The model numerical results of the circulations of the Red Sea (with its Spatial wind stress distribution, irregular coastal configuration and bottom topography) are presented in plots of mass-transport vectors and circulation streamlines.

2. Governing Equations

The continuity equation for the compressible flow, first derived by Leonhard Euler, [8] is

$$\frac{\partial \rho}{\partial t} + \frac{\partial(\rho u)}{\partial x} + \frac{\partial(\rho v)}{\partial y} + \frac{\partial(\rho v)}{\partial z} = 0, \tag{1}$$

where ρ is the fluid density, u, v, w are velocity components in x, y, z directions, and t is the time. Also, the momentum equation [6] in the Cartesian form is

$$\frac{\partial u}{\partial t} + u\frac{\partial u}{\partial x} + v\frac{\partial u}{\partial y} + w\frac{\partial u}{\partial z} = -\frac{1}{\rho}\frac{\partial p}{\partial x} + fv - 2\omega\cos\varphi w + \mu_v\frac{\partial^2 u}{\partial z^2} + \mu_h\left(\frac{\partial^2 u}{\partial x^2} + \frac{\partial^2 u}{\partial y^2}\right), \tag{2a}$$

$$\frac{\partial v}{\partial t} + u\frac{\partial v}{\partial x} + v\frac{\partial v}{\partial y} + w\frac{\partial v}{\partial z} = -\frac{1}{\rho}\frac{\partial p}{\partial y} + fu + \mu_v\frac{\partial^2 v}{\partial z^2} + \mu_h\left(\frac{\partial^2 v}{\partial x^2} + \frac{\partial^2 v}{\partial y^2}\right), \tag{2b}$$

$$\frac{\partial w}{\partial t} + u\frac{\partial w}{\partial x} + v\frac{\partial w}{\partial y} + w\frac{\partial w}{\partial z} = -\frac{1}{\rho}\frac{\partial p}{\partial z} - g - 2\omega\cos\varphi u + \mu_v\frac{\partial^2 w}{\partial z^2} + \mu_h\left(\frac{\partial^2 w}{\partial x^2} + \frac{\partial^2 w}{\partial y^2}\right), \tag{2c}$$

where p is the pressure field, x, y, z are Cartesian coordinate system fixed with respect to the rotating earth, with z upward, and f is the Coriolis parameter. μ_h, μ_v are depth averaged coefficients that model the momentum exchange due to eddies generated by the lateral turbulent and vertical mixing respectively, and φ is latitudinal angle.

3. Model Assumptions

To build a model of the Red Sea circulation, we assume the following.

(1) The time variations on the daily, weekly, and monthly scales are averaged. Consequently, all physical quantities are seasonally averaged and the flow is considered "quasi-steady"

$$\frac{\partial}{\partial t} = 0. \tag{3}$$

(2) Turbulent shear forces in the momentum equation ((2a), (2b), and (2c)) are simulated by depth averaged eddy (momentum exchange) coefficients μ_h, μ_v for lateral turbulent and vertical mixing, respectively. These coefficients have constant values.

(3) All types of wave –like and small-scale motions are neglected. Only current motion and large scale circulation are considered.

(4) The sea water density is assumed homogenous and hence density currents are neglected.

(5) The atmospheric pressure is assumed uniform over the Red Sea.

(6) The flow is assumed incompressible the vertical profile of the pressure field is assumed to be hydrostatic. Vertical acceleration is neglected.

(7) The Red Sea basin latitudinal extent is large enough to allow the Coriolis force and its latitude variation (the beta effect) to have a significant effect.

(8) Linearization is achieved by assuming the convective (non-linear) acceleration much smaller than the Coriolis (linear) acceleration [8].

4. Barotropic Model Equations

According to the model assumptions, the governing equations take the form [4, 6],

$$\frac{\partial u}{\partial x} + \frac{\partial v}{\partial y} + \frac{\partial w}{\partial z} = 0, \tag{4}$$

$$-fv = -\frac{1}{\rho}\frac{\partial p}{\partial x} + \mu_v\frac{\partial^2 u}{\partial z^2} + \mu_h\left(\frac{\partial^2 u}{\partial x^2} + \frac{\partial^2 u}{\partial y^2}\right), \tag{5}$$

$$fu = -\frac{1}{\rho}\frac{\partial p}{\partial y} + \mu_v\frac{\partial^2 v}{\partial z^2} + \mu_h\left(\frac{\partial^2 v}{\partial x^2} + \frac{\partial^2 v}{\partial y^2}\right), \tag{6}$$

$$\frac{\partial p}{\partial z} = -\rho g. \tag{7}$$

This set of linear partial equations in u, v, w and p are subject to boundary conditions; a wind stress at the mean sea surface, $z = 0$, and a frictional stress at the sea bottom, $z = -H$

$$\left(\tau_x^w, \tau_y^w\right) = \mu_v\left(\frac{\partial u}{\partial z}, \frac{\partial v}{\partial z}\right)_{z=0}, \quad \left(\tau_x^b, \tau_y^b\right) = \mu_v\left(\frac{\partial u}{\partial z}, \frac{\partial v}{\partial z}\right)_{z=-H}. \tag{8}$$

Define the components of mass transport between the sea surface, ζ, and the bottom, $-H$, in the x- and y-directions as

$$M_x = \int_{-H}^{\zeta} u dz, \qquad M_y = \int_{-H}^{\zeta} v dz. \tag{9}$$

Integrating equation (4) over z between the boundaries $-H(x, y)$ and $\zeta(x, y)$, and using the conditions of integrity of the free surface and impermeability of the bottom [5, 6],

$$\frac{\partial M_x}{\partial x} + \frac{\partial M_y}{\partial y} = 0. \tag{10}$$

A mass transport stream function $\psi(x, y)$ can then be defined

$$M_x = \frac{\partial \psi}{\partial y}, \qquad M_y = -\frac{\partial \psi}{\partial x}. \tag{11}$$

Integration of (7) over z between the boundaries $-H(x,y)$ and $\zeta(x,y)$ gives

$$p = p_a + \rho g(\zeta + H), \tag{12}$$

where p_a is the atmospheric pressure.

Integration of (5) and (6) over z between the boundaries $-H(x,y)$ and $\zeta(x,y)$ gives

$$\begin{aligned} -fM_y = &-\frac{1}{\rho}\frac{\partial}{\partial x}\int_{-H}^{\zeta} p\,dz + \mu_v\left(\left(\frac{\partial u}{\partial z}\right)_{\zeta} - \left(\frac{\partial u}{\partial z}\right)_{-H}\right) \\ &+ \mu_h\left(\frac{\partial^2 M_x}{\partial x^2} + \frac{\partial^2 M_x}{\partial y^2}\right), \end{aligned} \tag{13}$$

$$\begin{aligned} fM_x = &-\frac{1}{\rho}\frac{\partial}{\partial y}\int_{-H}^{\zeta} p\,dz + \mu_v\left(\left(\frac{\partial v}{\partial z}\right)_{\zeta} - \left(\frac{\partial v}{\partial z}\right)_{-H}\right) \\ &+ \mu_h\left(\frac{\partial^2 M_y}{\partial x^2} + \frac{\partial^2 M_y}{\partial y^2}\right). \end{aligned} \tag{14}$$

Dividing both equations by H differentiating (13) for y and (14) for x, and subtracting to eliminate pressure from the governing equations,

$$\begin{aligned} &\frac{\partial}{\partial x}\left(\frac{f}{H}\right)M_x + \frac{\partial}{\partial y}\left(\frac{f}{H}\right)M_y \\ &\quad = \left(-\frac{\partial}{\partial y}\left(\frac{\tau_x^w}{H}\right) + \frac{\partial}{\partial y}\left(\frac{\tau_x^b}{H}\right)\right. \\ &\qquad \left. + \frac{\partial}{\partial x}\left(\frac{\tau_y^w}{H}\right) - \frac{\partial}{\partial x}\left(\frac{\tau_y^b}{H}\right)\right) \\ &\qquad + \mu_h\left(\frac{\partial}{\partial x}\left(\frac{1}{H}\frac{\partial^2 M_y}{\partial x^2} + \frac{1}{H}\frac{\partial^2 M_y}{\partial y^2}\right)\right. \\ &\qquad \left. - \frac{\partial}{\partial y}\left(\frac{1}{H}\frac{\partial^2 M_x}{\partial x^2} + \frac{1}{H}\frac{\partial^2 M_x}{\partial y^2}\right)\right). \end{aligned} \tag{15}$$

It can be easily simplified to be

$$\begin{aligned} &\frac{-\mu_h}{H^2}\left[H\left(\frac{\partial^4\psi}{\partial x^4} + 2\frac{\partial^4\psi}{\partial x^2\partial y^2} + \frac{\partial^4\psi}{\partial y^4}\right)\right. \\ &\quad \left. - \frac{\partial H}{\partial x}\left(\frac{\partial^3\psi}{\partial x^3} + \frac{\partial^3\psi}{\partial x\partial y^2}\right) - \frac{\partial H}{\partial y}\left(\frac{\partial^3\psi}{\partial y^3} + \frac{\partial^3\psi}{\partial y\partial x^2}\right)\right] \\ &\quad + \frac{f}{H^2}\frac{\partial H}{\partial x}\frac{\partial\psi}{\partial y} - \left(\frac{\beta}{H} - \frac{f}{H^2}\frac{\partial H}{\partial y}\right)\frac{\partial\psi}{\partial x} \\ &= \left[\left(\frac{1}{H}\frac{\partial\tau_y^w}{\partial x} - \frac{\tau_y^w}{H^2}\frac{\partial H}{\partial x}\right) - \left(\frac{1}{H}\frac{\partial\tau_x^w}{\partial y} - \frac{\tau_x^w}{H^2}\frac{\partial H}{\partial y}\right)\right. \\ &\quad \left. + \left(\frac{1}{H}\frac{\partial\tau_y^b}{\partial x} - \frac{\tau_y^b}{H^2}\frac{\partial H}{\partial x}\right) - \left(\frac{1}{H}\frac{\partial\tau_x^b}{\partial y} - \frac{\tau_x^b}{H^2}\frac{\partial H}{\partial y}\right)\right]. \end{aligned} \tag{16}$$

Following the common assumption of the turbulent shear stress as linear function of horizontal mass transport [6, 7], using $\tau_x^b = cM_x$ and $\tau_y^b = cM_y$ in (16) leads to

$$\begin{aligned} &\frac{-\mu_h}{H^2}\left[H\left(\frac{\partial^4\psi}{\partial x^4} + 2\frac{\partial^4\psi}{\partial x^2\partial y^2} + \frac{\partial^4\psi}{\partial y^4}\right) - \frac{\partial H}{\partial x}\left(\frac{\partial^3\psi}{\partial x^3} + \frac{\partial^3\psi}{\partial x\partial y^2}\right)\right. \\ &\quad \left. - \frac{\partial H}{\partial y}\left(\frac{\partial^3\psi}{\partial y^3} + \frac{\partial^3\psi}{\partial y\partial x^2}\right)\right] \\ &\quad + \frac{c}{H}\left(\frac{\partial^2\psi}{\partial x^2} + \frac{\partial^2\psi}{\partial y^2}\right) + \left(\frac{f}{H^2}\frac{\partial H}{\partial x} - \frac{c}{H^2}\frac{\partial H}{\partial y}\right)\frac{\partial\psi}{\partial y} \\ &\quad - \left(\frac{\beta}{H} - \frac{f}{H^2}\frac{\partial H}{\partial y} - \frac{c}{H^2}\frac{\partial H}{\partial x}\right)\frac{\partial\psi}{\partial x} \\ &= \left(\frac{1}{H}\frac{\partial\tau_y^w}{\partial x} - \frac{\tau_y^w}{H^2}\frac{\partial H}{\partial x}\right) - \left(\frac{1}{H}\frac{\partial\tau_x^w}{\partial y} - \frac{\tau_x^w}{H^2}\frac{\partial H}{\partial y}\right), \end{aligned} \tag{17}$$

where c is the bottom friction coefficient with the value taken to be either .0025 or .005, depending on the author. Studies [8, 9] have used 0.0025, whereas [10] has used a value of 0.005. Rao and Murty [11] have used values 0.0025, 0.0125, and 0.000625 in the modeling of the Lake Ontario. They found that as the bottom friction coefficient decreased the maximum mass transport increased.

Two independent methods have been used for the solution of the simultaneous set of inhomogeneous equations presented by (17). The first one is an exact method called the LU-decomposition method [12]. The second is an iterative method called the Liebmann accelerated point over-relaxation method [13]. The LU-decomposition method does not involve any iteration procedures and is consequently more accurate than the relaxation method; it may not be suitable for multilayer situations and for more sophisticated models than the present one simply because of computer storage limitations in dealing with large matrices. For this reason we used the LU-decomposition method to be more accurate.

5. Numerical Solution

When the basin is rectangular with sides parallel to grid lines, the standard difference replacements can be applied at all internal grid points. When the basin is non-rectangular, this is the default of all real basins; internal grid points adjacent to the boundary require special treatment. Such a grid point is depicted in Figure 1. Expanding the spatial derivatives using the methods of [12, 14] of (17) will lead to a 13-point finite difference equation of ψ:

$$\begin{aligned} &C_1\psi_{i-2,j} + C_2\psi_{i-1,j} + C_3\psi_{i,j} + C_4\psi_{i+1,j} + C_5\psi_{i+2,j} \\ &\quad + C_6\psi_{i-1,j+1} + C_7\psi_{i-1,j-1} + C_8\psi_{i,j+1} + C_9\psi_{i,j-1} \\ &\quad + C_{10}\psi_{i,j+2} + C_{11}\psi_{i,j-2} + C_{12}\psi_{i+1,j+1} \\ &\quad + C_{13}\psi_{i+1,j-1} = \text{RHS}, \end{aligned} \tag{18}$$

where

$$C_1 = \frac{-\mu_h}{H_{i-2,j}^2}\left(\left(\frac{-6(s_3-2s_1-s_5)}{h^3 s_7(s_7+s_3)H_1H_2}\right)\left(\frac{\partial H}{\partial x}\right)_{i-2,j} + \frac{24H_{i-2,j}}{h^4 s_7(s_7+s_3)H_1H_2}\right),$$

$$C_2 = \frac{-\mu_h}{H_{i-1,j}^2}\left(\left(\frac{6(s_7+s_3-2s_1-s_5)}{h^3 s_7 s_3(s_7+s_3)(H_2-s_7)} + \frac{2(b_2+b_4)}{h(s_1+s_3)}\right)\left(\frac{\partial H}{\partial x}\right)_{i-1,j} - H_{i-1,j}\left(\frac{24}{h^4 s_7 s_3(s_7+s_3)(H_2-s_7)} + 4b_3(b_2+b_4)\right)\right.$$
$$\left. + \frac{cb_3}{H_{i-1,j}} + \frac{1}{h(s_1+s_3)}\left(\frac{\beta}{H_{i-1,j}} - \frac{f}{H_{i,j}^2}\left(\frac{\partial H}{\partial y}\right)_{i-1,j} - \frac{c}{H_{i-1,j}^2}\left(\frac{\partial H}{\partial x}\right)_{i-1,j}\right)\right),$$

$$C_3 = \frac{-\mu_h}{H_{i,j}^2}\left(H_{i,j}\left(\frac{24}{h^4 s_2 s_4(s_8+s_4)(s_2+s_6)} + \frac{24}{h^4 s_1 s_3(s_7+s_3)(s_1+s_5)} + (b_2+b_4)(b_1+b_3)\right) - \left(\frac{\partial H}{\partial x}\right)_{i,j}\right.$$
$$\left. \times\left(\frac{6(s_7+2s_3-2s_1-s_5)}{h^3 s_1 s_3(s_7+s_3)(s_1+s_5)}\right) - \left(\frac{\partial H}{\partial y}\right)_{i,j}\left(\frac{6(s_8+2s_4-2s_2-s_6)}{h^3 s_2 s_4(s_8+s_4)(s_2+s_6)}\right)\right) - \frac{2c}{H_{i,j}}(b_1+b_3+b_2+b_4),$$

$$C_4 = \frac{-\mu_h}{H_{i+1,j}^2}\left(\left(-\frac{6(s_7+2s_3-s_1-s_5)}{h^3 s_1 s_5(s_1+s_3)H_1} - \frac{2(b_2+b_4)}{h(s_1+s_3)}\right)\left(\frac{\partial H}{\partial x}\right)_{i+1,j} - H_{i+1,j}\left(\frac{24}{h^4 s_1 s_5(s_1+s_3)H_1} + 4b_1(b_2+b_4)\right)\right.$$
$$\left. + \frac{cb_1}{H_{i+1,j}} - \frac{1}{h(s_1+s_3)}\left(\frac{\beta}{H_{i+1,j}} - \frac{f}{H_{i,j}^2}\left(\frac{\partial H}{\partial y}\right)_{i+1,j} - \frac{c}{H_{i+1,j}^2}\left(\frac{\partial H}{\partial x}\right)_{i+1,j}\right)\right),$$

$$C_5 = \frac{-\mu_h}{H_{i+2,j}^2}\left(\left(\frac{6(s_7+2s_3-s_1)}{h^3 H_2(H_2-s_7)(s_1+s_5)s_5}\right)\left(\frac{\partial H}{\partial x}\right)_{i+2,j} + \frac{24H_{i+2,j}}{h^4 H_2(H_2-s_7)(s_1+s_5)s_5}\right),$$

$$C_6 = \frac{-\mu_h}{H_{i-1,j+1}^2}\left(2b_2b_3H_{i-1,j+1} - \left(\frac{b_2}{h(s_1+s_3)}\right)\left(\frac{\partial H}{\partial x}\right)_{i-1,j+1} - \left(\frac{\partial H}{\partial y}\right)_{i-1,j+1}\left(\frac{b_3}{h(s_2+s_4)}\right)\right),$$

$$C_7 = \frac{-\mu_h}{H_{i-1,j-1}^2}\left(2b_4b_3H_{i-1,j-1} - \left(\frac{b_4}{h(s_1+s_3)}\right)\left(\frac{\partial H}{\partial x}\right)_{i-1,j-1} - \left(\frac{\partial H}{\partial y}\right)_{i-1,j-1}\left(\frac{b_3}{h(s_2+s_4)}\right)\right),$$

$$C_8 = \frac{-\mu_h}{H_{i,j+1}^2}\left(H_{i,j+1}\left(\frac{-24}{h^4 s_2 s_6(s_2+s_4)H_1} - 4b_2(b_1+b_3)\right) + \left(\frac{\partial H}{\partial y}\right)_{i,j+1}\left(\frac{6(s_8+2s_4-s_2-s_6)}{h^3 s_2 s_6(s_2+s_4)H_3} + \frac{2(b_1+b_3)}{h(s_2+s_4)}\right)\right)$$
$$+ \frac{2cb_2}{H_{i,j+1}} + \left(\frac{f}{H_{i,j+1}^2}\left(\frac{\partial H}{\partial x}\right)_{i,j+1} - \frac{c}{H_{i,j+1}^2}\left(\frac{\partial H}{\partial y}\right)_{i,j+1}\right)\left(\frac{1}{h(s_2+s_4)}\right),$$

$$C_9 = \frac{-\mu_h}{H_{i,j-1}^2}\left(H_{i,j-1}\left(-\frac{24}{h^4 s_8 s_4(s_8+s_4)(H_4-s_8)} - 4b_4(b_1+b_3)\right) + \left(\frac{\partial H}{\partial y}\right)_{i,j-1}\left(\frac{6(s_8+s_4-2s_2-s_6)}{h^3 s_8 s_4(s_8+s_4)(H_4-s_8)} - \frac{2(b_1+b_3)}{h(s_2+s_4)}\right)\right)$$
$$+ \frac{2cb_4}{H_{i,j-1}} - \left(\frac{f}{H_{i,j-1}^2}\left(\frac{\partial H}{\partial x}\right)_{i,j-1} - \frac{c}{H_{i,j-1}^2}\left(\frac{\partial H}{\partial y}\right)_{i,j-1}\right)\left(\frac{1}{h(s_2+s_4)}\right),$$

$$C_{10} = \frac{-\mu_h}{H_{i,j+2}^2}\left(\left(\frac{-6(s_8+2s_4-s_2)}{h^3 H_4(H_4-s_8)(s_2+s_6)s_6}\right)\left(\frac{\partial H}{\partial x}\right)_{i,j+2} + \frac{24H_{i,j+2}}{h^4 H_2(H_2-s_7)(s_1+s_5)s_5}\right),$$

$$C_{11} = \frac{-\mu_h}{H_{i,j-2}^2}\left(\left(\frac{-6(s_4-2s_2-s_6)}{h^3 s_8(s_8+s_4)H_3H_4}\right)\left(\frac{\partial H}{\partial x}\right)_{i,j-2} + \frac{24H_{i,j-2}}{h^4 s_8(s_8+s_4)H_3H_4}\right),$$

$$C_{12} = \frac{-\mu_h}{H_{i+1,j+1}^2}\left(2b_2b_1H_{i+1,j+1} - \left(\frac{b_2}{h(s_1+s_3)}\right)\left(\frac{\partial H}{\partial x}\right)_{i+1,j+1} - \left(\frac{\partial H}{\partial y}\right)_{i+1,j+1}\left(\frac{b_1}{h(s_2+s_4)}\right)\right),$$

$$C_{13} = \frac{-\mu_h}{H_{i+1,j-1}^2}\left(2b_4b_1H_{i+1,j-1} - \left(\frac{b_4}{h(s_1+s_3)}\right)\left(\frac{\partial H}{\partial x}\right)_{i+1,j-1} - \left(\frac{\partial H}{\partial y}\right)_{i+1,j-1}\left(\frac{b_1}{h(s_2+s_4)}\right)\right),$$
$$\text{RHS} = \left(\frac{1}{H}\frac{\partial \tau_y^w}{\partial x} - \frac{\tau_y^w}{H^2}\frac{\partial H}{\partial x}\right)_{i,j} - \left(\frac{1}{H}\frac{\partial \tau_x^w}{\partial y} - \frac{\tau_x^w}{H^2}\frac{\partial H}{\partial y}\right)_{i,j}. \tag{19}$$

Where

$$\begin{aligned} b_1 &= \frac{2}{s_1(s_1+s_3)} \\ b_2 &= \frac{2}{s_2(s_2+s_4)} \\ b_3 &= \frac{2}{s_3(s_1+s_3)} \\ b_4 &= \frac{2}{s_4(s_2+s_4)} \\ b_0 &= b_1 + b_2 + b_3 + b_4. \end{aligned} \tag{20}$$

6. Boundary Conditions

Equation (18) is of fourth order in x, y, and one must satisfy eight lateral boundary conditions. Thus, $\Sigma(x, y)$ is the closed coastal boundary, we can set [15]

$$\psi = 0 \text{ on } \Sigma. \tag{21}$$

Additionally, we can stipulate no slip condition

$$\frac{\partial \psi}{\partial n} = 0 \text{ on } \Sigma. \tag{22}$$

7. Analytical Verifications

In this section the model is verified versus the analytical solution of Stommel over a rectangular domain with constant depth. The verification for variable depth will be carried against results of Alan and John [3].

7.1. Verifications against Stommel. Stommel retained the bottom friction terms to derive his model. The bottom friction was indeed the dissipative ingredient in the famous paper by Stommel [2] who first recognized the need to introduce dissipation into the system to obtain closed streamlines [15].

Stommel [2] assumed a distribution of wind stress of the form

$$\tau_x^w = -\tau_o \cos\frac{\pi y}{L}, \qquad \tau_{y=0}^w, \tag{23}$$

wind stress curl is zero at $y = 0$ and L, the southern and northern extents of a closed basin of extent L in the latitudinal direction and extent B in the longitudinal direction.

Define the small perturbation parameter $\varepsilon = \delta/W$ to represent the ratio of boundary layer thickness to the width of the basin. The solution of the Stommel problem is obtained by asymptotic expansion as [16]

$$\begin{aligned} \psi(x, y) &= \frac{\pi B \tau_o}{\beta L}\left(\frac{x}{B} - 1 + e^{-ax}\right)\sin\left(\frac{\pi y}{L}\right), \\ M_y &= -\frac{\pi B \tau_o}{\beta L}\left(\frac{1}{B} - ae^{-ax}\right)\sin\left(\frac{\pi y}{L}\right). \end{aligned} \tag{24}$$

where $a = \beta/c$. The analytical and numerical solutions are compared for the two values 0.025, 0.05 for parameter ε. Figure 2 shows analytical and numerical solutions of ψ for the value 0.05. Also, Figure 3 compares between the analytical and numerical solutions M_y for the value 0.05. The results are for typical values of $\tau_o = 0.1\,\text{Nm}^{-2}$, $W = 4000\,\text{km}$, $L = 4000\,\text{km}$, $\beta = 2 * 10^{-11}\,\text{m}^{-1}\,\text{s}^{-1}$, and $c = 2 * 10^{-6}\,\text{s}^{-1}$.

It is seen that the values of M_y are not zeros at western and eastern boundaries because the horizontal friction is neglected.

7.2. Verifications against Alan and John [3]. To verify the model over irregular bathymetry we shall considered the simplified model of the Lake Ontario basin used by Lockner [17]. It is an elliptic shoreline with a major axis of 300 km and a minor axis of 87 km, and sloping uniformly everywhere toward a maximum depth of 180 m in the center, Figure 4.

The basin is subjected to uniform wind stress opposite to the x-direction. The streamlines from the numerical solution (Figure 5) are perfectly as the results obtained by Alan and John [3]. Although the wind has zero curl, a double-gyre pattern appeared mainly due to depth variation. Depth variation is a main characteristic of real seas.

8. Circulations of the Red Sea

8.1. The Red Sea Wind Distribution. Wind velocity data were obtained for each region of the Red Sea for every month of the year. That is, monthly averaged regional mean wind velocity vectors were used. A monthly mean wind is assumed to flow persistently through the entire month. A regional mean wind is assumed to blow uniformly over the areal extent of the associated region. The Red Sea and its adjacent coasts were simulated by a rectangle 300 km wide and 2040 km long. This rectangle is subdivided into 17 Regions, each has a rectangular form with 300 km × 120 km. regions were numbered from south to north. Table 1 represents monthly mean values of the longitudinal surface wind velocity, while Table 2 represents monthly mean values of the latitudinal surface wind velocity [18].

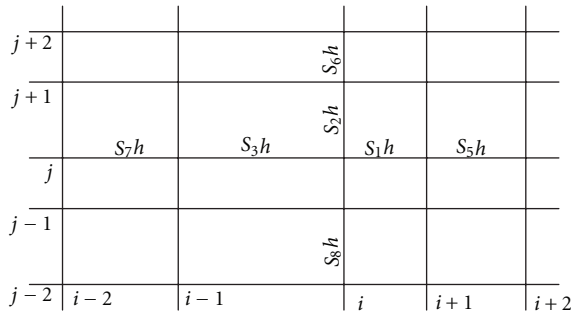

Figure 1: Schematic grid diagram.

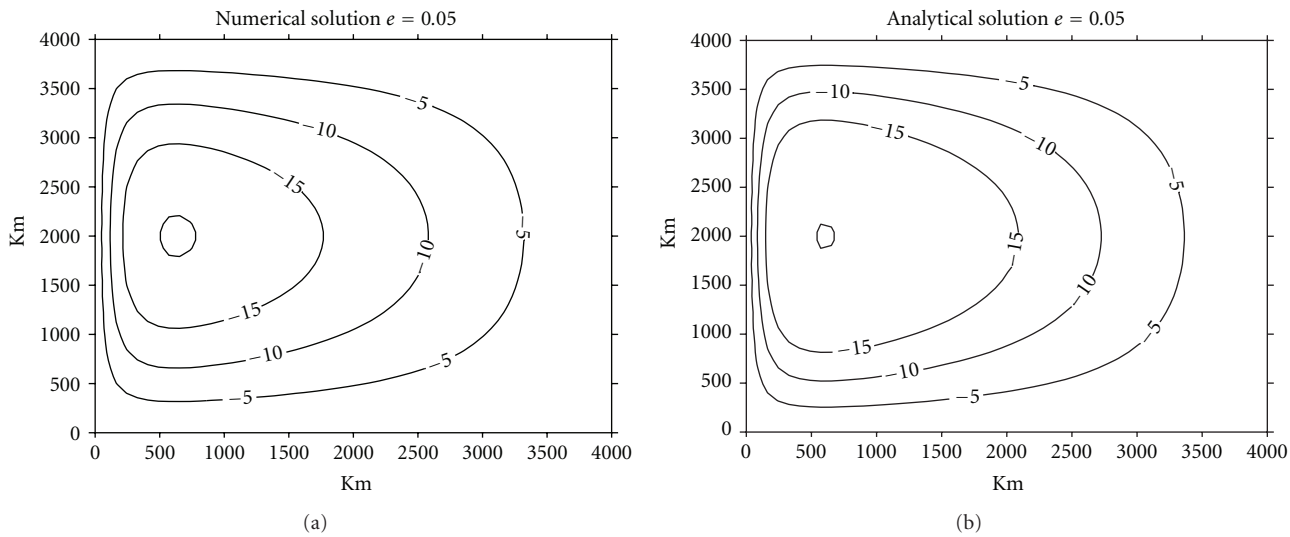

Figure 2: Numerical and analytical streamlines in a flat-bottom rectangular ocean for the Stommel problem $\varepsilon = 0.05$.

Table 1: Monthly mean values of the longitudinal surface wind velocity (m/s).

	Jan.	Feb.	Mar.	Apr.	May	Jun.	Jul.	Aug.	Sept.	oct.	Nov.	Dec.
1	4.4	4.4	2.4	2.4	2.4	−0.1	−2.4	−2.4	−0.9	4.4	4.4	4.4
2	4.4	4.4	4.4	2.4	2.4	−0.1	−2.4	−2.4	−0.9	4.4	4.4	6.7
3	6.7	6.7	6.7	4.4	2.4	−0.9	−2.4	−2.4	−0.9	4.4	9.3	9.3
4	6.7	4.4	4.4	2.4	0.9	−0.9	−0.9	−0.9	−0.9	4.4	6.7	6.7
5	4.4	2.4	2.4	0.9	0	−2.4	−0.9	−0.9	−0.9	2.4	4.4	4.4
6	2.4	0.9	0.9	0.1	0.1	−2.4	−2.4	−0.9	−0.9	0.9	4.4	2.4
7	0.9	0	0	0.1	0.9	−2.4	−2.4	−0.4	−0.9	0	2.4	2.4
8	−0.9	−0.9	−0.9	−0.9	−0.9	−4.4	−2.4	−2.4	−2.4	0	−0.9	−0.9
9	−0.9	−2.4	−0.9	−0.9	−2.4	−4.4	−2.4	−2.4	−2.4	0	−0.9	−0.9
10	−2.4	−2.4	−2.4	−2.4	−2.4	−4.4	−2.4	−2.4	−2.4	−2.4	−0.9	−2.4
11	−2.4	−4.4	−2.4	−2.4	−2.4	−4.4	−2.4	−2.4	−2.4	2.4	−2.4	−2.4
12	−2.4	−4.4	−2.4	−2.4	−2.4	−4.4	−2.4	−2.4	−4.4	−2.4	−2.4	−2.4
13	−4.4	−4.4	−4	−2.4	−2.4	−4.4	−2.4	−2.4	−4.4	−2.4	−2.4	−2.4
14	−4.4	−4.4	−4.4	−2.4	−4.4	−4.4	−2.4	−2.4	−4.4	−4.4	−4.4	−2.4
15	−4.4	−4.4	−4.4	−4.4	−4.4	−4.4	−4.4	−4.4	−6.7	−4.4	−4.4	−4.4
16	−4.4	−4.4	−4.4	−4.4	−4.4	−6.7	−6.7	−6.7	−9.3	−6.7	−4.4	−4.4
17	−4.4	−4.4	−4.4	−4.4	−6.7	−6.7	−6.7	−6.7	−6.7	−6.7	−4.4	−4.4

Table 2: Monthly mean values of the latitudinal surface wind velocity (m/s).

	Jan.	Feb.	Mar.	Apr.	May	Jun.	Jul.	Aug.	Sept.	oct.	Nov.	Dec.
1	−2.9	−2.9	−1.03	1	0.6	0	0.6	0.4	−0.15	−1.76	−4.4	−4.4
2	−2.9	−2.9	−1.88	2.1	0.6	0	0.6	0.4	−0.15	−1.76	−4.4	−6.7
3	−4.4	−4.4	−2.88	2.1	0.6	0.2	0.6	0.4	−0.15	−1.76	−9.3	−9.3
4	−4.4	−2.9	−1.9	1	0.2	0.2	0.2	0.15	0.15	−1.76	−6.7	−6.7
5	−2.9	−1.6	−1.03	0.4	0	0.6	0.15	0.15	0.15	0.96	−4.4	−4.4
6	−1.6	0.6	−0.4	0	0	0.6	0.4	0.15	0.15	0.36	−4.4	−2.4
7	−0.6	0	0	0	0.2	0.6	0.4	0.4	0.15	0	−2.4	−0.9
8	0.6	0.6	0.4	0.4	0.2	1.1	0.4	0.4	0.4	0	−0.9	−2.4
9	0.6	1.6	0.4	0.4	0.6	1.1	0.4	0.4	0.4	0	−0.9	−0.9
10	1.6	1.6	1	1	0.6	1.1	0.4	0.4	0.4	0.96	0.9	2.4
11	1.6	1.6	1	1	0.6	1.1	0.6	0.4	0.7	0.96	2.4	2.4
12	1.6	2.9	1	1	0.6	1.1	0.6	0.6	0.7	0.96	2.4	2.4
13	2.9	2.9	1.9	1	0.6	1.1	0.6	0.4	0.7	0.96	2.4	2.4
14	2.9	2.9	1.9	1	1.1	1.1	0.6	0.4	0.7	1.76	4.4	2.4
15	2.9	2.9	1.9	1.9	1.1	1.7	0.7	0.7	1.1	1.76	4.4	4.4
16	2.9	2.9	1.9	1.9	1.1	1.7	1.1	1.1	1.55	2.7	4.4	4.4
17	2.9	2.9	2.1	2.1	1.7	1.7	1.1	1.1	1.1	2.6	4.4	4.4

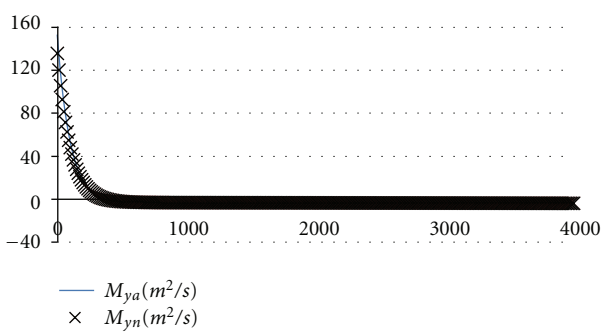

Figure 3: Numerical and analytical M_y in a flat-bottom rectangular ocean for the Stommel problem $\varepsilon = 0.05$.

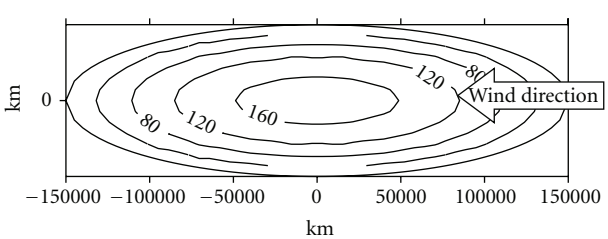

Figure 4: Depth contours for the simple elliptic basin.

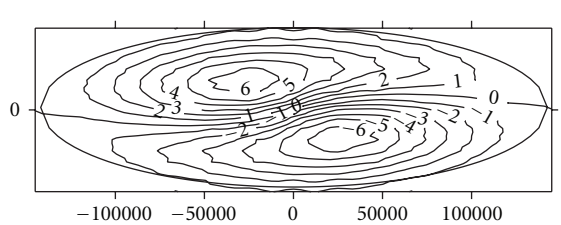

Figure 5: Streamline contours for the simple elliptic basin.

8.2. Momentum Transfer at Water Surface. When wind blows over a sea, it exerts a shearing stress on the water surface. Momentum is transferred from the wind to the surface and due to the turbulence transported further down into the water. Accurate knowledge of the force exerted by the wind on the water surface is a prerequisite for every attempt to analyze the movements of water. The formula used for determining the wind shear stress from a given wind speed is [3, 19]

$$\tau_x^w = \rho_a c_s W_x \sqrt{W_x^2 + W_y^2}, \qquad \tau_y^w = \rho_a c_s W_y \sqrt{W_x^2 + W_y^2}, \tag{25}$$

where c_s *is wind stress coefficient*, W_x, W_y, are the component wind speeds in x- and y-directions, respectively, and ρ_a is the air density. For ground surfaces the characteristic roughness is truly a characteristic of the surface. The water surface, however, changes character with increasing wind speed and becomes more corrugated. Also, the dimensions of a sea influence the characteristic roughness of the water. Although it may not be possible to truly define a roughness parameter of a sea, this parameter or rather the stress coefficient has been determined from wind measurements and from observations of the wind set-up. Wilson [7] has analyzed the literature on the stress coefficient over oceans and computed average values of the stress coefficient referred to as an elevation of 10 meters:

$$\begin{aligned} c_s &= 1.5 * 10^{-3} \pm 0.8 * 10^{-3} \quad \text{for } W < 6 \text{ m/s}, \\ c_s &= 2.4 * 10^{-3} \pm 0.6 * 10^{-3} \quad \text{for } W > 6 \text{ m/s}. \end{aligned} \tag{26}$$

From the Great Lakes of North America much lower values have been reported [20]. Observations indicated that an appropriate value for the Great Lakes is $1.2 * 10^{-3}$. Donelan et al. [21] estimated the wind stress from the steady-state water setup of Lake Ontario and found the wind stress coefficient to

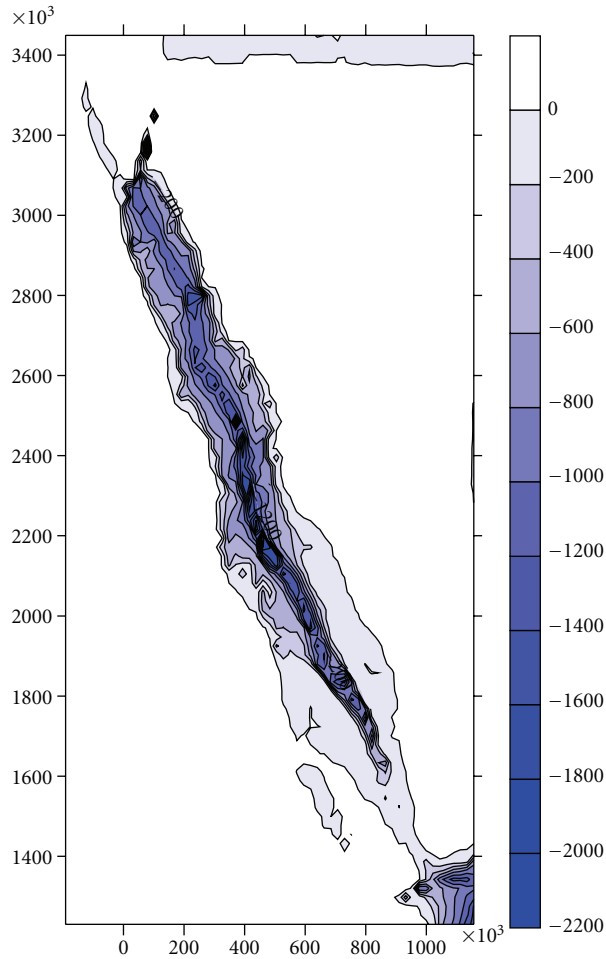

Figure 6: The Red Sea Basin.

be $1.3 * 10^{-3}$ for stable and neutral conditions and $1.6 * 10^{-3}$ for unstable conditions.

For enclosed water bodies and fetches of the order 10 km the reported values on the wind stress coefficient are scarce. Bengtsson [22] studied Lake Vomb in southern Sweden. It was found to use $1.2 * 10^{-3}$ for speeds higher than 5.5 m/s and $0.9 * 10^{-3}$ for speeds lower than 4.5 m/s. Alan and John [3] used a value of $2.7 * 10^{-3}$ in their simplified elliptic representation of the Lake Ontario. Shankar et al. [19] used a value of $2.55 * 10^{-3}$. In our simulation of the Red Sea a value of $2.0 * 10^{-3}$ is used.

8.3. The Red Sea Bottom Depth Distribution. The Red Sea long narrow basin separates Africa from Asia and extends from NNW to SSE between latitudes 12° 30′ N to 30° N, in an almost straight line. Its total length is 1932 km and average width is 280 km. In width it decreases from 306 km, near Massawa, to 26 km in the Straits of Bab Al Mandab.

The Red Sea latitude extent from 12° 30′ N to 30° N warrants an effective and variable Coriolis force, the $\beta-$effect [1]. The central channel reaches great depths of more than 2000 m. However, the average Red Sea depth is 450 m only. This central channel is fringed in the southern Red Sea by shallow areas less than 50 m deep. See Figure 6 that describes the Red Sea basin characteristics.

The area of the Red Sea is $4.6\times105\,\text{km}^2$ and its mean depth is 500 m. The maximum recorded depth is 3039 m in the axial trough at 19° 35′ N, 38° 40′ E. The Red Sea from the Gulf of Aden lies to the north of Bab Al Mandab near Hannish Island, where the channel is only about 130 m at its deepest.

9. The Red Sea Circulation and Mass Transport

The model can predict the Red Sea circulation driven by different wind distributions. The coefficient of bottom friction is taken as 0.0025. The output presented below included both the stream function and mass transport vectors. Simulations are carried for different cases, averaged values of summer, winter and also for of the entire year. Figures 7, 8, and 9 show the seasonally-averaged stream lines and mass transport vectors for winter, summer, and the whole year respectively. Each figure is composed of three distributions: (a) The driving wind stress distribution, (b) The resulting field of mass-transport vectors, and (c) The resulting pattern of circulation streamlines.

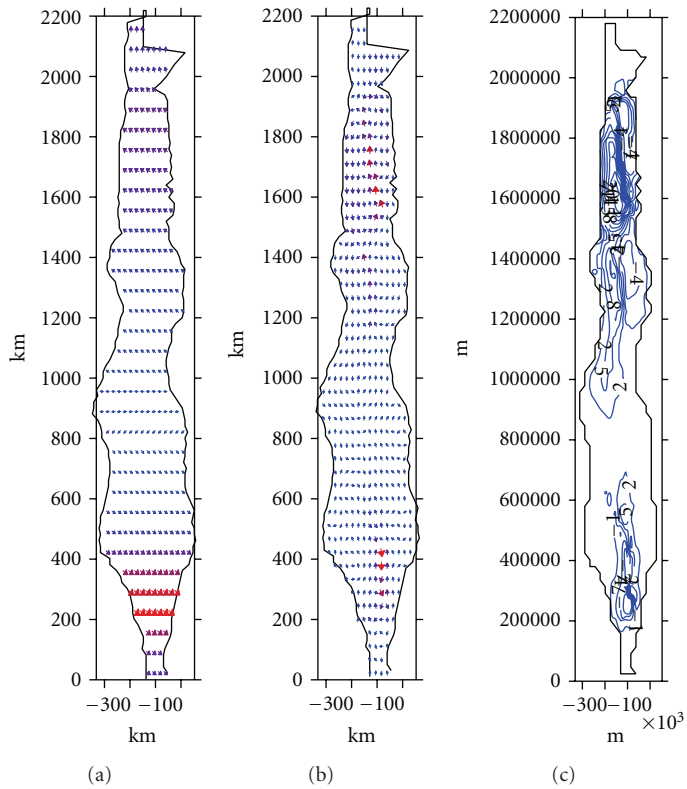

Figure 7: Wind stress vectors (a) mass transport vectors (b) and Streamlines (c) Values in the Red Sea are winter-averaged.

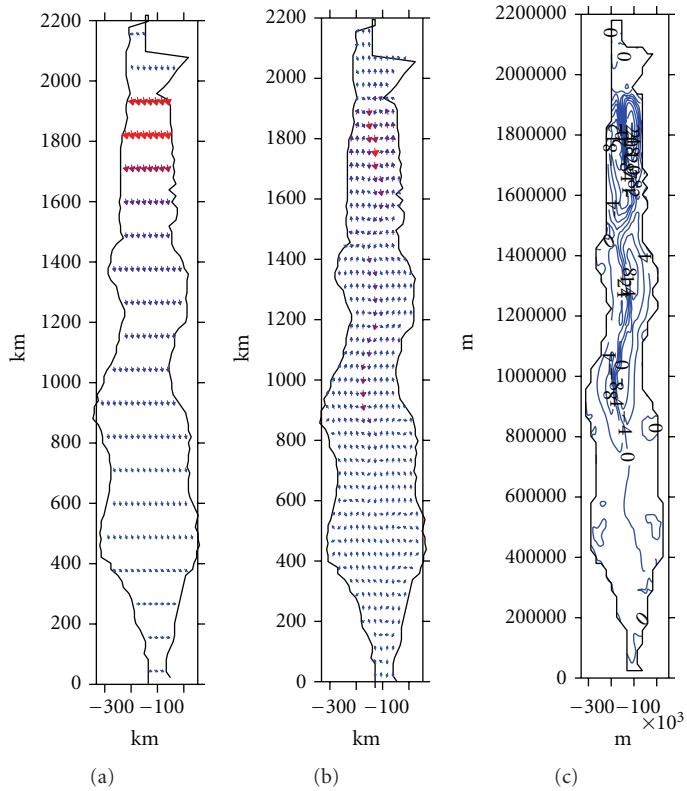

Figure 8: Wind stress vectors (a) mass transport vectors (b) and Streamlines (c) Values in the Red Sea are summer-averaged.

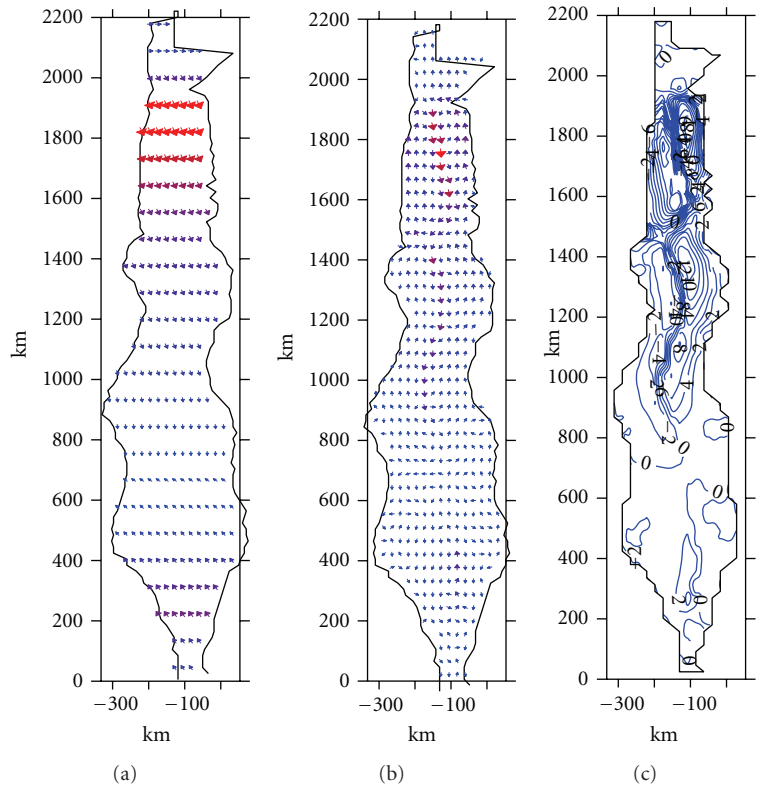

Figure 9: Wind stress vectors (a) mass transport vectors (b) and Streamlines (c) Values in the Red Sea are year-averaged.

These plots of seasonal Red Sea mass-transport vectors and streamlines demonstrate the manner by which they are influenced by the interaction of two patterns: the wind-stress pattern and the bottom-bathymetry pattern. The wind-driven circulation show some features which can be summarized bellow:

(1) The largest mass transport in all cases is in the deepest area in the Red sea. The central area is in the northern part.

(2) Mass transport direction is the same as wind direction along the central part and then circulates in the opposite direction beside the shoreline.

(3) The mass transport values in the northern part are much greater than the values in the southern part. Complex depth variations in the northern part cause this difference.

(4) The wind in the summer blows in the south-west direction over the total area but in the winter it blows in the south-west direction in the northern part and in the north-east direction in the southern part. As a result of this variation flow patterns are more complex in the winter than in the summer.

(5) The summer has a maximum value of streamline of 23 *Sverdrup* while the winter has a maximum value of 30 *Sverdrup* while the maximum value for the averaged-year simulation is 24 *Sverdrup*.

References

[1] M. A. F. M. Zaki, "Combined wind and density-driven circulation in enclosed seas with variable coriolis parameter," *Journal of Engineering and Applied Sciences*, vol. 42, pp. 433–446, 1995.

[2] H. Stommel, "The westward intensification of wind-diven ocean currents," *American Geophysical Union*, vol. 29, no. 2, 1948.

[3] J. W. Alan and H. T. John, "Steady wind driven currents in a large lake with depth-dependent eddy viscosity," *Journal of Physical Oceanography*, vol. 6, no. 1, 1976.

[4] W. Lick, "Numerical modelling of lake currents," *Annual Review of Fluid Mechanics*, vol. 4, pp. 49–74, 1976.

[5] L. H. Kantha and C. A. Clayson, *Numerical Models of Oceans and Oceanic Processes*, Academic Press, 2000.

[6] G. Neumann and W. J. Pierson, *Principles of Physical Oceanography*, Prentice-Hall, New Jersey, NJ, USA, 1966.

[7] B. W. Wilson, "Note on surface wind stress over water at low and high speeds," *Journal of Geophysical Research*, vol. 65, no. 10, pp. 3377–3382, 1960.

[8] P. D. Thompson, *Numerical Weather Analysis and Prediction*, Macmillan, New York, NY, USA, 1961.

[9] J. O. Backhaus and E. Maier-Reimer, "On seasonal circulation in the North Sea," in *North Sea Dynamics*, J. Sundermann and W. Lenz, Eds., p. 693, Springer, Heidelberg, Germany, 1983.

[10] G. K. Furnes, "Wind effects in the North Sea," *Journal of Physical Oceanography*, vol. 10, no. 6, pp. 978–984, 1980.

[11] D. B. Rao and T. S. Murty, "Calculation of the steady state wind-driven circulations in Lake Ontario," *Archiv für*

Meteorologie, Geophysik und Bioklimatologie Serie A, vol. 19, no. 2, pp. 195–210, 1970.

[12] A. R. Mitchell and D. F. Griffths, *Computational Methods in Partial Differential Equations*, John Wiley & Sons, New York, NY, USA, 1980.

[13] S. C. Chapra and R. P. Canale, *Numerical Methods for Engineers*, McGraw-Hill, 5th edition, 2006.

[14] A. K. Singh and B. S. Bhadauria, "Finite difference formulae for unequal sub-intervals using lagrange's interpolation formula," *International Journal of Mathematics and Analysis*, vol. 3, no. 17, pp. 815–827, 2009.

[15] G. L. Mellor, *Introduction to Physical Oceanography*, Springer, New York, NY, USA, 1996.

[16] M. Van Dyke, *Perturbation Methods in Fluid Mechanics*, Academic Press, New York, NY, USA, 1964.

[17] D. Lockner, "Sensitivity of a numerical circulation model of Lake Ontario to change in Lake Symmetry and friction depth and to variable wind stress," IFYGL. Rochester Embayment Project Report No. 2, Department of Geological Sciences, University of Rochester, 1973.

[18] M. A. F. M. Zaki and I. E. Mobarek, "A model of the Red Sea air pollution II- the computational model," *Scientific Engineering Bulletin, Faculty of Engineering, Cairo University*, vol. 2, 1981.

[19] N. J. Shankar, X. B. Chao, H. F. Cheong, and Y. Q. Li, "Numerical simulation of oil spills in the Singapore coastal waters," in *Recent Advances in Marine Science and Technology*, N. Saxena, Ed., pp. 177–188, PACON International, 2001.

[20] J. P. Bruce, D. V. Andersson, and G. K. Rodgers, "Temperature, humidity and wind profiles over the great lakes," in *Proceedings of the 4th Conference on Great Lakes Research*, pp. 65–70, 1961.

[21] M. A. Donelan, F. C. Elder, and P. F. Hamblin, "Determination of the aerodynamic drag coefficient from wind set-up," in *Proceedings of the 17th Conference on Great Lakes Research*, pp. 778–788, 1974.

[22] L. Bengtsson, *Wind Stress on Small Lakes*, Tekniska Högskolan, Lund, Sweden, 1973.